Cement and Concrete Composites 129 (2022) 104464

Contents lists available at ScienceDirect

Cement and Concrete Composites

journal homepage: www.elsevier.com/locate/cemconcomp

Ultra-high-strength engineered/strain-hardening cementitious composites (ECC/SHCC): Material design and effect of fiber hybridization

Bo-Tao Huang [a], Ji-Xiang Zhu [a], Ke-Fan Weng [a,b], Victor C. Li [c], Jian-Guo Dai [a,*]

[a] Department of Civil and Environmental Engineering, The Hong Kong Polytechnic University, Hong Kong, China
[b] Department of Ocean Science and Engineering, Southern University of Science and Technology, Shenzhen, Guangdong, China
[c] Department of Civil and Environmental Engineering, University of Michigan, Ann Arbor, USA

ARTICLE INFO

Keywords:
Engineered cementitious composites (ECC)
Strain-hardening cementitious composites (SHCC)
Ultra-high-performance concrete (UHPC)
Hybrid fiber
Multiple cracking

ABSTRACT

It is well known that an increase in the compressive strength of cementitious composites is usually accompanied by a loss of tensile ductility. Designing and developing ultra-high-strength cementitious composites (e.g., ≥200 MPa) with high tensile strain capacity (e.g., ≥3%) and excellent crack resistance (e.g., crack width ≤100 μm) remain challenging. In this study, a series of ultra-high-strength Engineered Cementitious Composites (UHS-ECC) with a compressive strength over 210 MPa, a tensile strain capacity of 3–6% (i.e., 300–600 times that of ordinary concrete), and a fine crack width of 67–81 μm (at the ultimate tensile strain) were achieved. Hybrid design of fiber reinforcement and matrix for UHS-ECC was adopted by combining the ECC and ultra-high-performance concrete (UHPC) design concepts, and the effect of fiber hybridization and aspect ratio on the mechanical behavior of UHS-ECC was comprehensively investigated. The overall performance of UHS-ECC was assessed and compared with the existing high-strength ECC and strain-hardening UHPC, and it was found that the currently designed UHS-ECC recorded the best overall performance among the existing materials. Finally, the multiple cracking behavior of UHS-ECC was analyzed and modeled based on a probabilistic approach to evaluate its critical tensile strain for durability control in practical applications. The results of this study have pushed the performance envelope of both ECC and UHPC materials and provided a basis for developing cementitious composites with simultaneously ultra-high compressive strength, ultra-high tensile ductility, and excellent crack resistance.

1. Introduction

Strength, ductility, and durability are always essential properties for concrete materials. Among the advanced concrete family, two types of cementitious materials have drawn particular attention worldwide in the recent two decades. The first is Engineered/Strain-Hardening Cementitious Composites (ECC/SHCC), a type of high-performance fiber-reinforced cementitious composites [1–5] designed based on micromechanical guidelines to realize significant strain-hardening and multiple-cracking behaviors under direct tension [6–8]. Generally, the tensile strain capacity of ECC is reported to range from 1% to 8% (i.e., 100–800 times that of ordinary concrete) [1,9], but the compressive strength is usually below 80 MPa [1,10]. The crack width of ECC in tension can be controlled below 100 μm under service loading, which may be self-healed under various environmental conditions [11–15]. Compared with ordinary plain or fiber-reinforced concrete, ECC show superior mechanical properties [16–18] and durability [19–21], which can be used in both existing structures and new construction to improve the resilience and sustainability of concrete infrastructure [22–25]. The second emerging cementitious material that has also drawn significant attention is Ultra-High-Performance Concrete (UHPC), which was reported to exhibit a high compressive strength of 150–250 MPa [26–31], high elastic modulus, and very dense microstructures. UHPC has also been used as an excellent material for both repair of existing concrete structures and new construction to improve the durability and reduce the self-weight [32–35]. Compared with ordinary ECC materials, UHPC shows a much higher strength but its tensile strain capacity is relatively low (typically below 1.0%) [27,29–31].

To achieve both high strength and high ductility of cementitious composites, high-strength ECC has been developed in recent years

* Corresponding author.
E-mail addresses: botaohuang@zju.edu.cn (B.-T. Huang), ji-xiang.zhu@connect.polyu.hk (J.-X. Zhu), ke-fan.weng@connect.polyu.hk (K.-F. Weng), vcli@umich.edu (V.C. Li), cejgdai@polyu.edu.hk (J.-G. Dai).

https://doi.org/10.1016/j.cemconcomp.2022.104464
Received 5 November 2021; Received in revised form 21 January 2022; Accepted 25 February 2022
Available online 3 March 2022

[36–49], including those produced using seawater and sea-sand together with non-corrosive reinforcement for marine concrete structures [4,50,51]. The compressive strength of existing high-strength ECC ranged from 80 to 170 MPa. It should be pointed out that polyvinyl alcohol (PVA) fibers are widely used for normal-strength ECC [1,2], while polyethylene (PE) and steel fibers are commonly used in high-strength ECC [38,52] and UHPC [27,32] owing to their superior fiber strength and modulus. The ECC developed by Ranade [38] had a compressive strength of 205 MPa (the highest among the existing ECC), a tensile strain capacity of 4.6%, but a comparatively large crack width in tension (i.e., 135 μm on average at the ultimate stage). Generally, a finer crack width is also critical for the durability performance of cementitious composites, and typically a crack width below 100 μm is desirable for achieving self-healing behavior of ECC [11,12].

Recently, the authors conducted a preliminary study to develop ultra-high-strength ECC (UHS-ECC) using hybrid fiber reinforcement, and had achieved a compressive strength of 211 MPa, a tensile strain capacity of 5.2%, and an average crack width of 72 μm (at the ultimate strain) [53]. Up to now, only two studies [38,53] reported ECC with a compressive strength over 170 MPa. Use of fiber hybridization has proved to be an efficient way to improve the mechanical behavior of ordinary fiber-reinforced concrete, normal/high-strength ECC, and UHPC (e.g. Refs. [52,54–58]). However, the material performance also relies on the property of cementitious matrix. There is still a significant lack of knowledge on how to design the hybrid fiber reinforcement together with an optimized cementitious matrix for developing UHS-ECC. In addition, understanding and modeling the cracking behavior of UHS-ECC at different strain levels are the basis for designing the crack-related mechanical and durability performance of UHS-ECC. However, no literature has been published on these critical issues.

In this study, a hybrid design procedure for the fiber reinforcement and matrix for UHS-ECC has been proposed to develop a series of UHS-ECC with the compressive strength over 210 MPa. The effects of fiber hybridization [i.e., hybrid PE and steel fibers] and aspect ratio on the mechanical properties of UHS-ECC were systematically investigated. The mechanical performance and cracking behavior of the formed UHS-ECC were assessed in comparison with the existing ECC and UHPC materials. In addition, the cracking behavior of UHS-ECC at different deformation levels was analyzed by digital image correlation (DIC) technique and simulated by a probabilistic-based approach.

2. Hybrid design of matrix and fiber reinforcement for UHS-ECC

In this section, the procedure for hybrid design of matrix and fiber reinforcement for UHS-ECC is introduced, followed by its mixing process and curing condition as well as the testing methods.

2.1. Hybrid matrix design

The matrix design of UHS-ECC was specifically formulated based on the material design guidelines of both ECC [1,6] and UHPC [26,59]. To achieve an ultra-high compressive strength and very dense microstructures, the paste materials (cement, silica fume, slag, and quartz powder) were selected and designed according to the cement chemistry and packing theory of UHPC [26,59]. Silica fume was used to remarkably enhance the strength and reduce the porosity of the matrix, owing to its fine particle size and high pozzolanic activity [60]. The silica fume-to-cement ratio was fixed at 0.25 as this ratio was widely used in UHPC with ultra-high strength [26,27]. Slag has been used in ECC materials with high tensile ductility [42]. Quartz powder was used to adjust the particle packing of the paste. In this study, the target cumulative passing of the paste was determined by the modified Andreasen and Andersen model [59,61].

$$P(D) = \left(D^q - D_{\min}^q\right) / \left(D_{\max}^q - D_{\min}^q\right) \quad (1)$$

where D is the particle size, $P(D)$ is a fraction of the total particles smaller than D, $D_{\max}$ is the maximum particle size, $D_{\min}$ is the minimum particle size, and q is the distribution modulus. In this study, the value of q was fixed at 0.23 [59].

For UHPC, the particle size distribution of silica sand is considered in the particle packing optimization, so that the sand-to-binder ratio of UHPC matrix is around 1.0. However, according to the design guideline of ECC [1,6], a comparatively low sand-to-binder ratio (commonly 0.25–0.30) is required to ensure a suitable fracture toughness of matrix [1,51]. Thus, for the UHS-ECC matrix, the content of silica sand was not considered here for the particle packing optimization, and the sand-to-binder ratio was set to 0.27. As fine silica sand is widely used in ECC materials, the silica sand with a mean particle size below 300 μm (Fig. 1) was used for UHS-ECC in the present study.

Based on the afore-mentioned design principals and the target cumulative passing of the paste [i.e., **Eq. (1)**], the mix proportion of the UHS-ECC matrix in Table 1 was obtained. Fig. 1 presents the particle size distributions of the raw materials and paste. The maximum particle sizes of all the paste materials (i.e., cement, silica fume, slag, and quartz powder) were less than 50 μm, and the SEM images of the paste materials are shown in Fig. 2. The tested cumulative passing of the final paste was very close to the target curve (i.e., the dashed line in Fig. 1). It should be pointed out that the cumulative passing of the paste between 0.5 and 2.0 μm was slightly higher than that of the target one because the silica fume-to-cement ratio was fixed to 0.25.

The raw materials and mix proportion of the designed UHS-ECC matrix are listed in Table 1, including cement (Type I 52.5 N Portland cement, BS EN 197–1:2011), silica fume (SiO_2 content over 93%), slag, quartz powder, silica sand, water, and polycarboxylate ether superplasticizer (solid form). The water-to-cementitious binder ratio was 0.158, the sand-to-binder ratio was 0.272, and the superplasticizer-to-binder ratio was 0.015. The chemical compositions of raw materials (cement, silica fume, slag, and quartz powder) are omitted here which were the same as used in the authors' preliminary study [53].

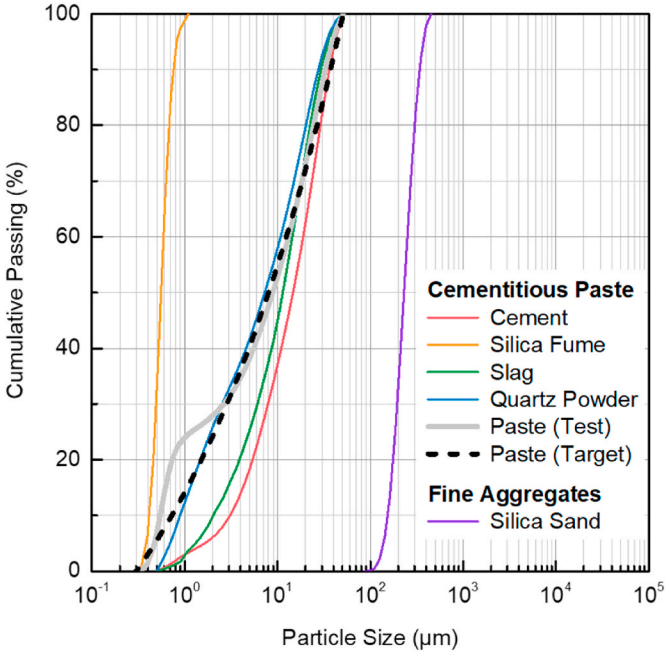

Fig. 1. Particle size distributions of raw materials and paste. The particle size distribution of the paste materials (cement, silica fume, slag, and quartz powder) was close to that of the target curve.

Table 1
Mix proportion of UHS-ECC matrix.

UHS-ECC Matrix	Cementitious Binder			Quartz Powder	Silica Sand	Water	Superplasticizer
	Cement	Silica Fume	Slag				
Weight ratio	1.000	0.250	0.125	0.125	0.375	0.218	0.020
Mass (kg/m^3)	1126	282	141	141	422	245	23

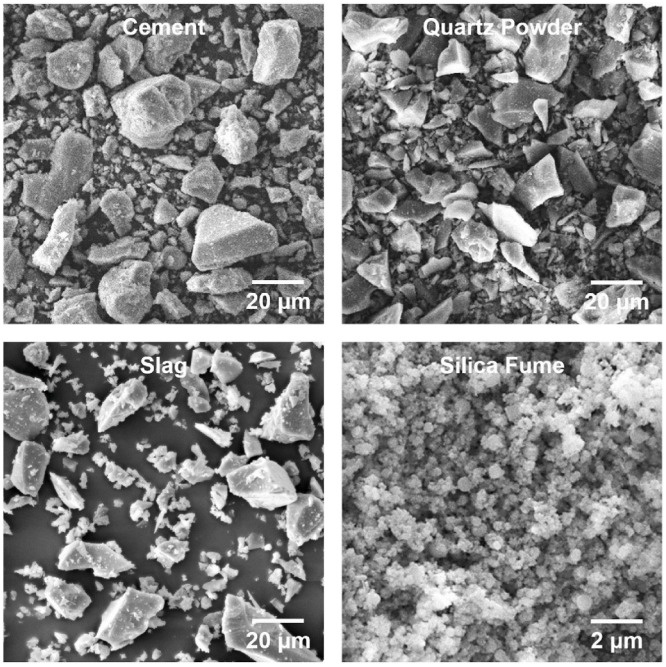

Fig. 2. SEM images of the raw materials used in the cementitious paste of UHS-ECC (cement, quartz powder, slag, and silica fume).

2.2. Hybrid fiber reinforcement design

For strain-hardening UHPC, 2–4% (Vol.) steel fibers were generally used to reinforce the matrix [27,29–31]. The high modulus of steel fiber (compared to synthetic fibers) leads to a fine crack width of strain-hardening UHPC (approximately 10–30 μm). For high-strength ECC, 2% (Vol.) ultra-high-molecular-weight (UHMW) PE fibers were used [4,37,45] to realize a high tensile strain capacity and the lengths of PE fibers were commonly 12–18 mm. The crack widths of high-strength ECC at the ultimate strain were commonly 60–200 μm, which are significantly larger than that of strain-hardening UHPC. In this study, to take the advantage of both steel and PE fibers, hybrid fiber reinforcement (steel and PE fibers) was used for UHS-ECC with a total fiber volume fraction of 3.0%. As the use of PE fibers significantly decreases the workability, the content of PE fibers in UHS-ECC was controlled no more than 2% (Vol.). To understand the effect of fiber hybridization and aspect ratio on the mechanical properties of UHS-ECC, a comprehensive experimental program was conducted to obtain an optimized hybrid design of fiber reinforcement for UHS-ECC.

Table 2 lists the properties of PE and steel fibers used in UHS-ECC. The PE fiber had the diameter and lengths of 24 μm and 12/18 mm, respectively. The straight steel fiber had the diameter and lengths of 200 μm and 13/20 mm, respectively. The aspect ratios of PE and steel fibers are also listed in Table 2. The photographs of the PE and steel fibers used are shown in Fig. 3.

Table 3 lists the mix IDs and fiber properties (i.e., length, aspect ratio, and content) of UHS-ECC. It is noted that the matrices of all the mixes were the same (Table 1). Taking **18**P2.0/**20**S1.0 for example, "**18**P2.0" means that the mix contained **18**-mm PE fibers with 2.0% volume fraction, and "**20**S1.0" means that the mix contained **20**-mm steel fibers with 1.0% volume fraction. The UHS-ECC in Table 3 are divided into two series (i.e., aspect-ratio series and fiber-hybridization series) and **12**P**2.0**/**13**S**1.0** is the common reference mix for the two series. It should be noted that the mixes of **12**P**2.0**/**13**S**1.0** and 12P**1.5**/13S**1.5** correspond to the mixes M-P2.0S1.0 and M-P1.5S1.5 in the authors' preliminary study [53], respectively.

2.3. Mixing process and curing condition

The following mixing process was used for UHS-ECC (1) the paste materials (i.e., cement, silica fume, slag, and quartz powder): and silica sand were dry mixed for 2–3 min; (b) the superplasticizer and water were added and mixed for 10–12 min; (c) the fibers were added and mixed for 5–6 min; and (d) the prepared mixture was cast into molds. The mini-slump spread diameter of the fresh UHS-ECC was measured according to ASTM C1437 [62]. For the aspect-ratio series, the spread diameters of **18**P2.0/**20**S1.0, **18**P2.0/**13**S1.0, **12**P2.0/**20**S1.0, and **12**P2.0/**13**S1.0 were 123, 125, 128, and 129 mm, respectively. It can be found that the longer PE (or steel) fibers resulted in slightly lower flowability of the fresh UHS-ECC. For the fiber-hybridization series, the spread diameter increased from 129 mm (**12**P**2.0**/**13**S**1.0**) to 177 mm (12P**0.0**/13S**3.0**) as the content of steel fiber increased. The developed UHS-ECC exhibited lower flowability than normal-strength ECC (approximately 250–350 mm [63]) and high-strength ECC (approximately 160–180 mm [51]). So, more efforts may be needed to improve the workability of UHS-ECC in the future. The completed UHS-ECC samples were stored at 20 °C for 24 h, demolded, and then cured in 90 °C water for 9 d [37,38]. The 90 °C heat curing can increase the pozzolanic activity of both silica fume and quartz powder and also increase the average chain length of C–S–H [64]. After the heat curing, UHS-ECC was placed at room temperature (20–24 °C). According to the prior trial tests before this study, after 9-day heat curing, the effect of curing time on the mechanical properties of UHS-ECC was very limited. Thus, to shorten the test cycle, the mechanical properties of UHS-ECC were determined 12 days after casting. It should be pointed out that the heat-cured UHS-ECC could be used in the structural members which are prefabricated in the factory. In future studies, the development of ambient-cured UHS-ECC is critical to broaden the practical application of this material.

Table 2
Properties of PE and steel fibers (obtained from manufactures).

Fiber	Diameter, d_f (μm)	Length, l_f (mm)	Aspect Ratio, l_f/d_f	Strength (MPa)	Modulus (GPa)	Density (g/cm^3)
PE fiber	24	12, 18	500, 750	3000	100	0.97
Steel fiber	200	13, 20	65, 100	≥2000	210	7.8

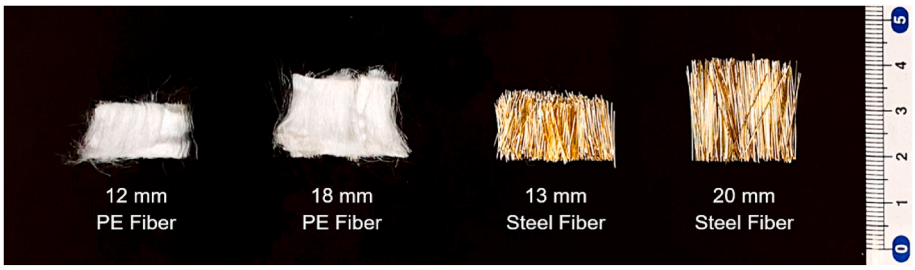

Fig. 3. Photographs of PE and steel fibers.

Table 3
Mix IDs of UHS-ECC.

Mix ID	PE fiber			Steel fiber			Note
	Length (mm)	Aspect Ratio	Content (Vol. %)	Length (mm)	Aspect Ratio	Content (Vol. %)	
18P2.0/**20**S1.0	**18**	750	2.0	**20**	100	1.0	Aspect-Ratio Series
18P2.0/**13**S1.0	**18**	750	2.0	**13**	65	1.0	Aspect-Ratio Series
12P2.0/**20**S1.0	**12**	500	2.0	**20**	100	1.0	Aspect-Ratio Series
12P2.0/13S1.0	**12**	500	**2.0**	**13**	65	**1.0**	Aspect-Ratio & Fiber-Hybridization Series (Common Mix)
12P**1.5**/13S**1.5**	12	500	**1.5**	13	65	**1.5**	Fiber-Hybridization Series
12P**1.0**/13S**2.0**	12	500	**1.0**	13	65	**2.0**	Fiber-Hybridization Series
12P**0.5**/13S**2.5**	12	500	**0.5**	13	65	**2.5**	Fiber-Hybridization Series
12P**0.0**/13S**3.0**	12	500	**0**	13	65	**3.0**	Fiber-Hybridization Series

2.4. Testing methods

The compressive strength of UHS-ECC was determined using 50 mm × 50 mm × 50 mm cubes, according to ASTM C109/C109 M [65]. The tensile properties of UHS-ECC were determined using dumbbell samples (Fig. 4, loading rate 0.5 mm/min), according to JSCE's recommendation [66]. The tensile deformation of the central part (80-mm length) was measured using a linear variable differential transformer. Digital image correlation (DIC) was used to analyze the tensile strain field and cracking behavior of UHS-ECC [24,67,68]. The speckle pattern for DIC analysis was applied on the middle part of the specimen (Fig. 4). During the test, digital images were captured every 3 s, and the image resolution was approximately 15 μm per pixel. Based on the DIC results, the widths of all the tensile cracks in the central part of the specimen were calculated and analyzed. After the test, the fiber failure modes on the tensile fracture surface of UHS-ECC were observed using SEM (Tescan VEGA3).

3. Mechanical properties of UHS-ECC

3.1. Compressive strength

Fig. 5 presents the compressive strengths of the developed UHS-ECC, which were over 210 MPa. For the aspect-ratio series, the aspect ratios of PE and steel fibers had a marginal effect on the compressive strength of UHS-ECC. For the fiber-hybridization series, as the PE fiber content decreased and the steel fiber content increased, the compressive strength of UHS-ECC increased. This phenomenon is consistent with the trend for normal-strength ECC (around 35 MPa) with polyvinyl alcohol (PVA) and steel fibers (total volume content 2.5%) [58] and high-strength ECC (around 125 MPa) reinforced with PE and steel fibers (total volume content 2.0%) [52]. Owing to the higher modulus and load capacity of steel fiber, replacing PE fiber by steel fiber can improve the compressive strength of ECC [52]. In addition, higher PE fiber content may result in a higher pore volume in the matrix, which could be attributed to the worm effect of PE fibers that created more pores in the matrix [69]. It should be noted that for ECC with a compressive strength from 30 MPa to 90 MPa, the compressive strength of 100-mm cube is approximately 0.96 that of 50-mm cube [70]. For UHS-ECC, the size

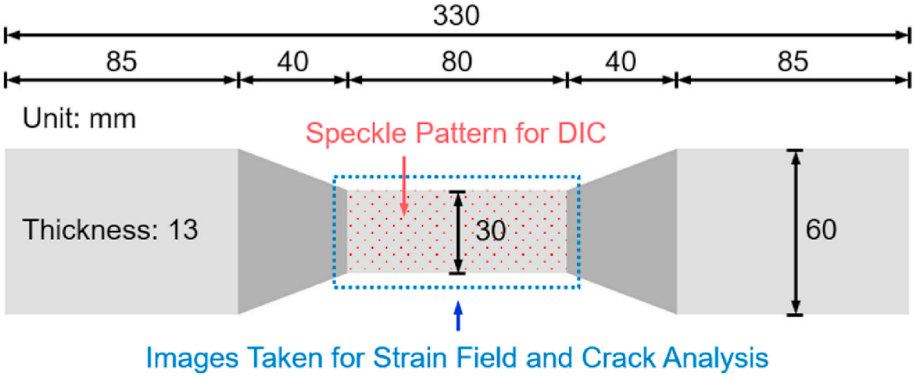

Fig. 4. Specimen for direct tension test.

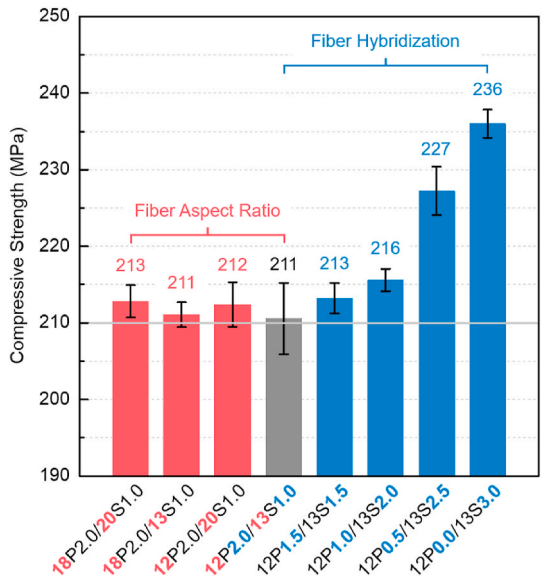

Fig. 5. Compressive strengths of the developed UHS-ECC (all over 210 MPa). The compressive strength increased with increasing steel fiber content; and the aspect ratios of PE and steel fibers had a marginal effect on the compressive strength.

effect of the compressive strength remains unclear and needs to be investigated in future study.

3.2. Tensile performance

The tensile stress–strain curves of UHS-ECC are presented in Fig. 6, and the tensile properties are summarized in Fig. 7a and Fig. 7b. In Fig. 6, tensile strain-hardening behavior can be observed for all the mixes studied. The tensile strengths of all the mixes (Fig. 7a) were close (ranging from 15.5 MPa to 17.7 MPa). Compared to the mixes with 13-mm steel fibers (**18**P2.0/**13**S1.0 and **12**P2.0/**13**S1.0), the mixes with 20-mm steel fibers (**18**P2.0/**20**S1.0 and **12**P2.0/**20**S1.0) showed a slightly higher tensile strength (i.e., 17.7 MPa). Fig. 7b summarizes the tensile strain capacities of the UHS-ECC. The mixes with PE fiber content of 2.0% and 1.5% had a tensile strain capacity over 3%, and **18**P2.0/**13**S1.0 showed the highest tensile strain capacity of 6.3%. For the aspect-ratio series, the mixes with 13-mm steel fibers showed higher tensile ductility than those with 20-mm steel fibers. For the fiber-hybridization series, as the PE fiber content decreased and steel fiber content increased, the tensile strain capacity of UHS-ECC decreased. The similar trend was reported in high-strength ECC with hybrid PE and steel fibers [52], and it was also found that when the PE fiber content decreased from 1.5% to 1.0%, the tensile strain capacity of high-strength ECC decreased significantly. The tensile strain capacities of 12P**1.0**/13S**2.0** (Figs. 6f), 12P**0.5**/13S**2.5** (Figs. 6h), and 12P**0.0**/13S**3.0** (Fig. 6g) were less than 1%. For the UHS-ECC with a steel fiber content higher than 2.0% (PE fiber lower than 1.0%), the crack width and number of UHS-ECC decreased (see ***Section 4***), which

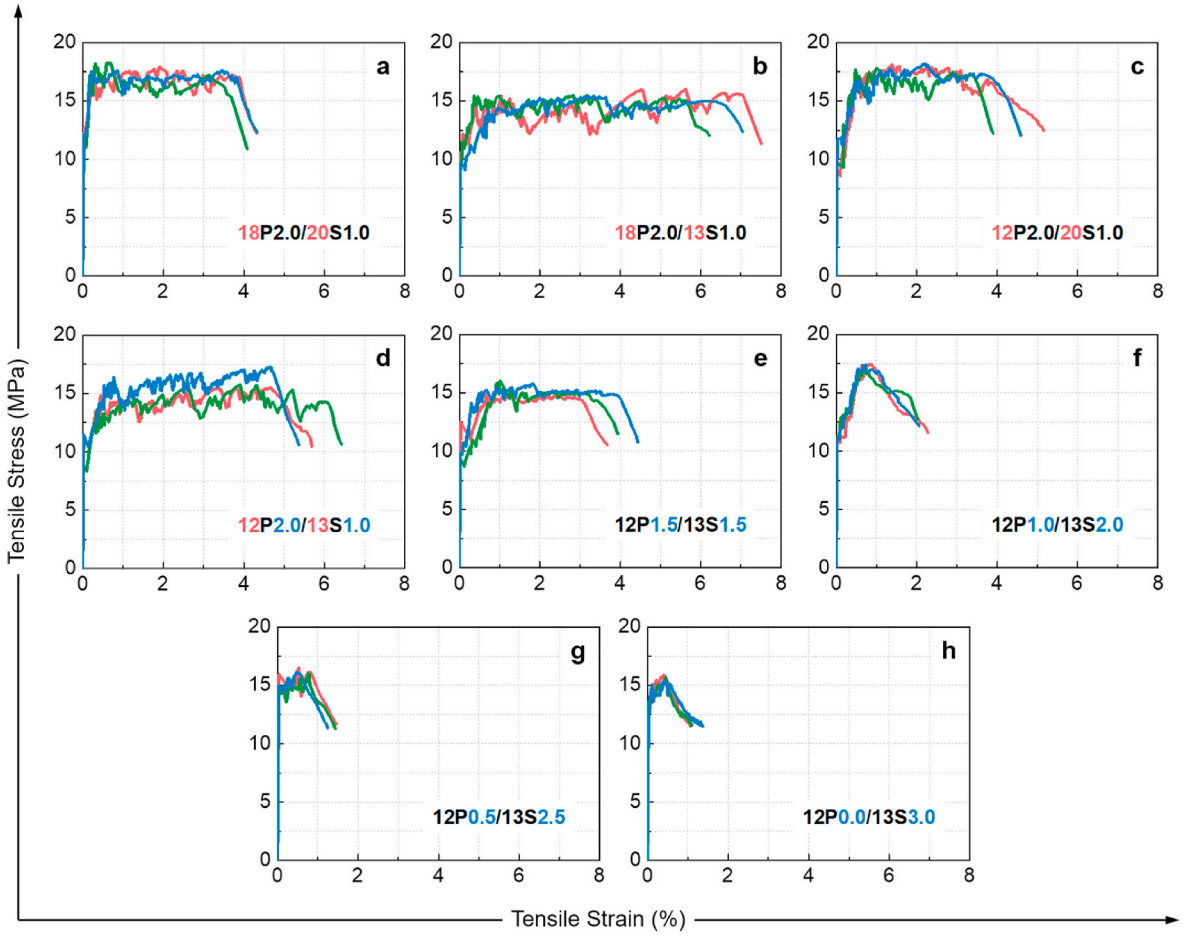

Fig. 6. Tensile stress–strain curves of UHS-ECC. Tensile strain-hardening behavior can be observed for the developed UHS-ECC, and the UHS-ECC with 2.0% PE fiber and 1.0% steel fiber (a–d) showed superior tensile ductility.

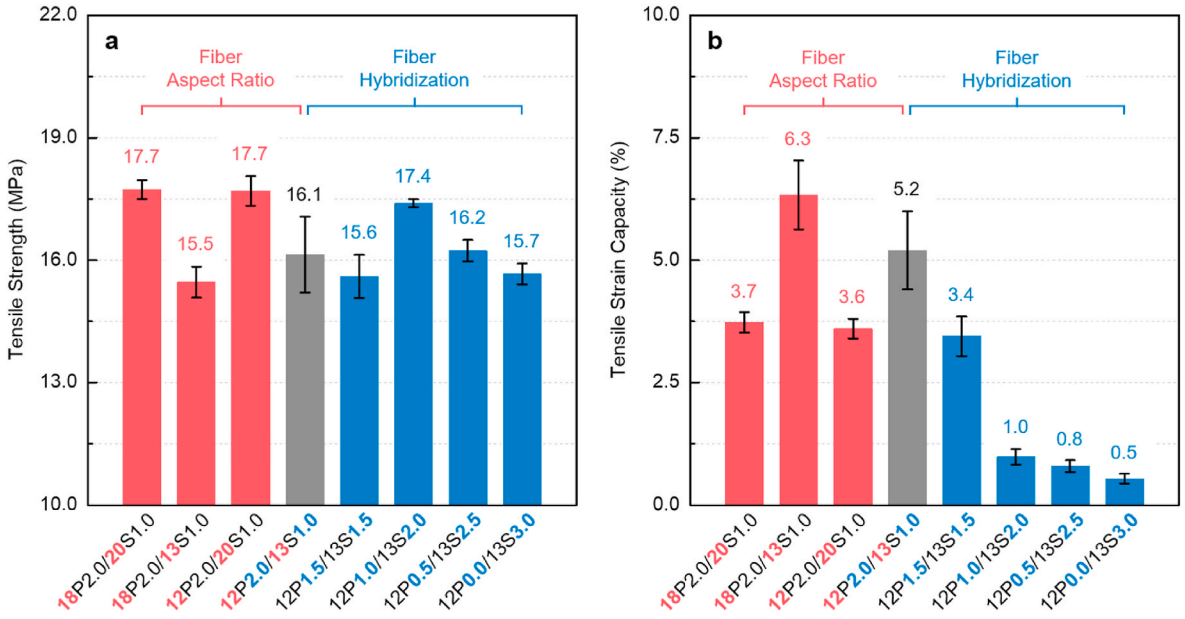

Fig. 7. Tensile (a) strength and (b) strain capacity of UHS-ECC. UHS-ECC with 20-mm steel fibers (**18**P2.0/**20**S1.0 and **12**P2.0/**20**S1.0) showed the highest tensile strength (17.7 MPa), and **18**P2.0/**13**S1.0 showed the highest tensile strain capacity (6.3%).

corresponded to the comparatively low tensile strain capacity. Actually, the tensile strain capacities of 12P**1.0**/13S**2.0**, 12P**0.5**/13S**2.5**, and 12P**0.0**/13S**3.0** were slightly higher than or close to that of UHPC. Thus, it may be more precise to classify these three mixes as strain-hardening UHPC instead of UHS-ECC.

3.3. Fiber failure mode

Fig. 8 presents the typical SEM images of the tensile fracture surface of UHS-ECC with hybrid fiber reinforcement. The fiber failure modes are presented in Fig. 8a. The pullout failure was observed for steel fibers, while both rupture and pullout failures were observed for PE fibers. The rupture of some amount of PE fibers indicated that the strength of PE fiber was effectively used in the ultra-high strength matrix. Compared to the PE fibers, the steel fibers had higher modulus and tensile capacity (Table 2), so that only the pullout failure occurred. In Fig. 8b, the trace of pulled-out PE and steel fibers are marked with dashed lines. In addition, some traces of friction can be observed on the surface of PE fibers (Fig. 8c), meaning that the dense matrix of UHS-ECC resulted in strong bond and friction between the fiber and the matrix. Consequently, the strong fiber/matrix bond led to the rupture of some PE fibers on the failure surface.

4. Cracking behavior and performance assessment

4.1. Crack patterns and DIC results

Fig. 9 shows the crack patterns and DIC results of the UHS-ECC mixes. For each selected sample, the strain fields at four different deformation levels are presented. The first deformation level was set as 0.20%, the last deformation level was set as the ultimate tensile strain, and the other two deformation levels divided the strain range between 0.2% and the ultimate strain into thirds. In the DIC results, the cracking area increased with increasing tensile deformation levels, and multiple cracking behavior was significant for all the mixes studied. Compared to the UHS-ECC with a tensile strain capacity over 3% (Fig. 9a–e), the other mixes (Fig. 9f–h) showed lower local strain values, resulting in smaller local crack widths. In addition, the mixes with 2% PE fibers and 1% steel fibers (Fig. 9a–d) showed more saturated multiple cracking than the other mixes (Fig. 9e–h), and **18**P2.0/**13**S1.0 showed the most saturated cracking behavior among all mixes. These observations are consistent with the tensile strain capacities of UHS-ECC shown in Fig. 7b.

According to the method in Ref. [4], the crack width at the ultimate tensile strain was obtained based on the high-resolution digital image of each sample. In Table 4 and Fig. 10a, the average crack widths (w) at the

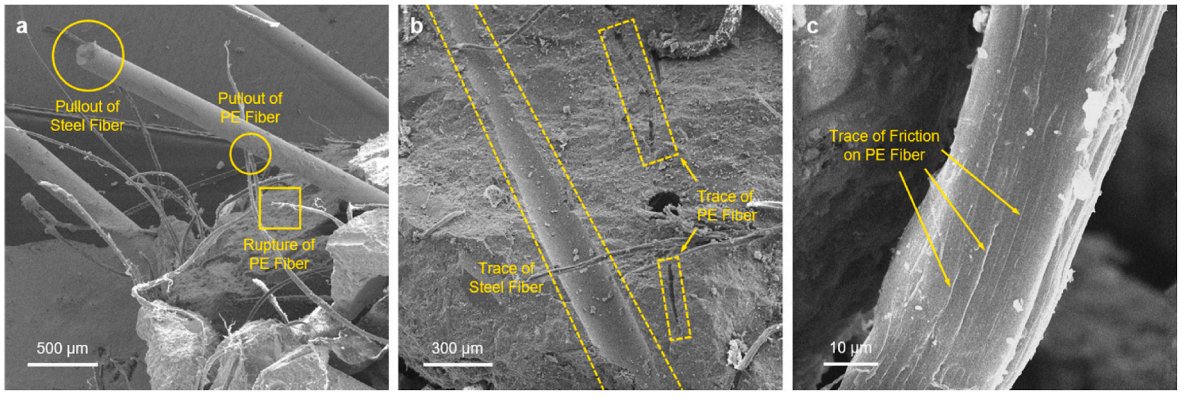

Fig. 8. Typical SEM images of the tensile fracture surface of UHS-ECC: (a) fiber failure modes, (b) traces of steel and PE fiber grooves, and (c) trace of friction-induced damage on PE fiber. The pullout failure was observed for steel fibers, while both rupture and pullout failures were observed for PE fibers.

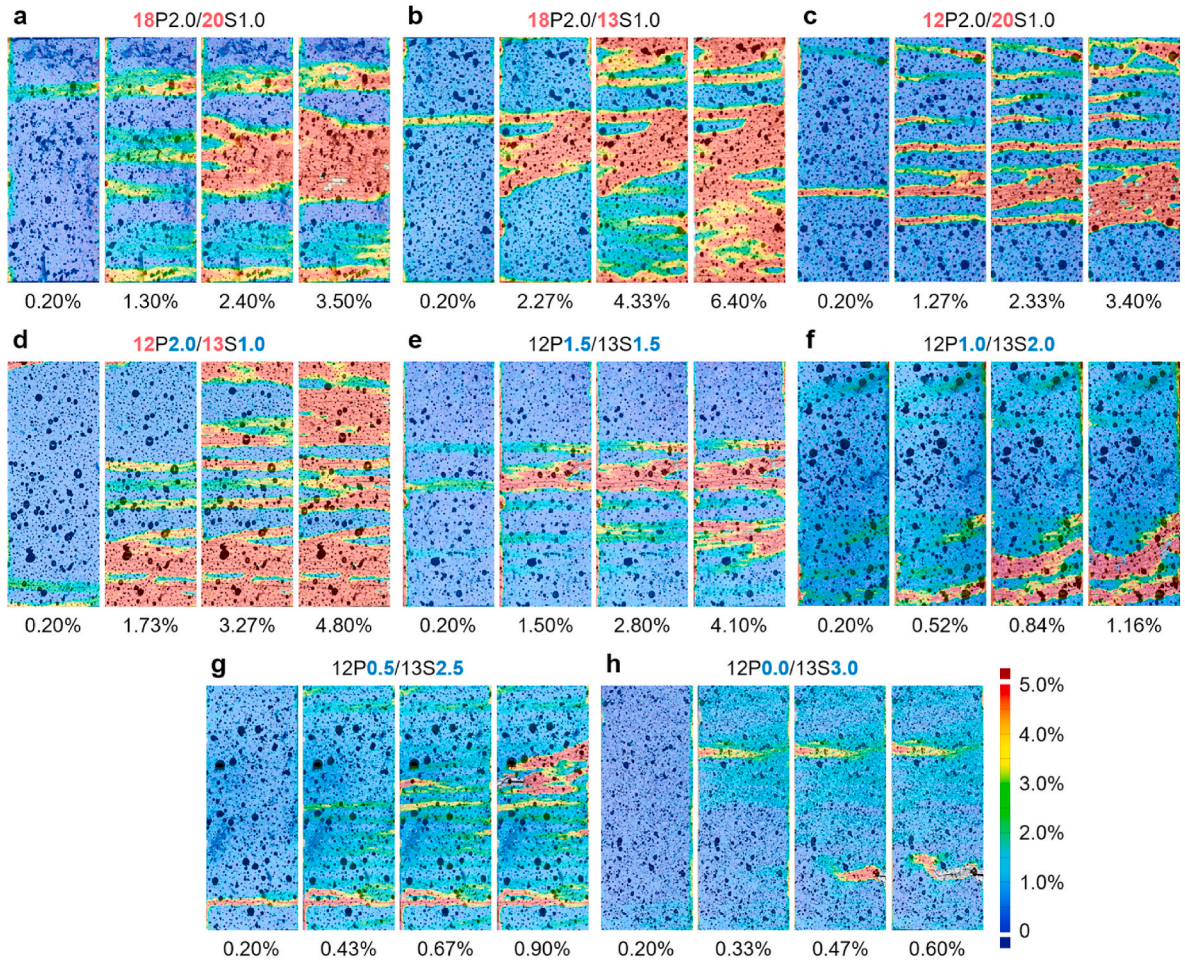

Fig. 9. DIC results of UHS-ECC strain fields at different deformation levels. Multiple cracking behavior can be observed for all the developed UHS-ECC.

Table 4
Average values of the mechanical properties of UHS-ECC.

Material ID	Compressive Strength, f'_c (MPa)	Tensile Strain Capacity, ε_t (%)	Tensile Strength, f_t (MPa)	Crack Width, w (μm)	Standard Deviation of Crack Widths, s_w (μm)	$f'_c f_t \varepsilon_t / w$ Index (MPa^2/μm)
18P2.0/**20**S1.0	213 ± 2.1	3.7 ± 0.2	17.7 ± 0.2	81 ± 4	32 ± 13	1.73
18P2.0/**13**S1.0	211 ± 1.6	6.3 ± 0.7	15.5 ± 0.4	68 ± 2	26 ± 5	3.02
12P2.0/**20**S1.0	212 ± 2.9	3.6 ± 0.2	17.7 ± 0.4	67 ± 10	28 ± 6	2.02
12P2.0/13S1.0	211 ± 4.7	5.2 ± 0.8	16.1 ± 0.9	72 ± 3	27 ± 3	2.45
12P**1.5**/13S**1.5**	213 ± 2.0	3.4 ± 0.4	15.6 ± 0.5	112 ± 10	36 ± 15	1.02
12P**1.0**/13S**2.0**	217 ± 1.4	1.0 ± 0.2	17.4 ± 0.1	51 ± 16	26 ± 9	0.73
12P**0.5**/13S**2.5**	227 ± 3.2	0.8 ± 0.1	16.2 ± 0.3	53 ± 7	32 ± 5	0.55
12P**0.0**/13S**3.0**	236 ± 1.8	0.5 ± 0.1	15.7 ± 0.3	45 ± 8	31 ± 8	0.44

ultimate tensile strain of all the samples are below 90 μm except for 12P**1.5**/13S**1.5**. In addition, the mixes with steel fiber content ≥2% showed smaller crack widths (45–53 μm), due to the higher modulus of steel fibers. The standard deviation of crack widths at the ultimate tensile strain (s_w) is also calculated and summarized in Table 4 and Fig. 10b, which is useful to evaluate the multiple-cracking behavior of UHS-ECC (i.e., the smaller s_w means more stable multiple-cracking behavior) [4]. It can be found in Fig. 10b that the fiber aspect ratio and hybridization had marginal effect on the standard deviation of crack widths of UHS-ECC. The crack width distributions at different deformation levels will be further analyzed and modeled in ***Section 6***.

4.2. *Five-dimensional diagram for UHS-ECC performance*

A five-dimensional diagram was introduced by Huang et al. [4] to assess the mechanical performance (i.e., compressive strength f'_c, tensile strain capacity ε_t, and tensile strength f_t) and cracking behavior at the ultimate tensile strain (i.e., average crack width w and standard deviation of crack widths s_w) of strain-hardening cementitious composites. For the UHS-ECC mixes studied, the five-dimensional diagrams of the mechanical and cracking performance are shown in Fig. 11. Here smaller crack width (w) and crack width deviation (s_w) mean better durability performance and more stable multiple cracking behavior. To get a positive correlation between the cracking parameter values and the cracking performance, the reciprocals of w and s_w (i.e., $1/w$ and $1/s_w$) are used. In Fig. 11a and b, all values are normalized by the corresponding

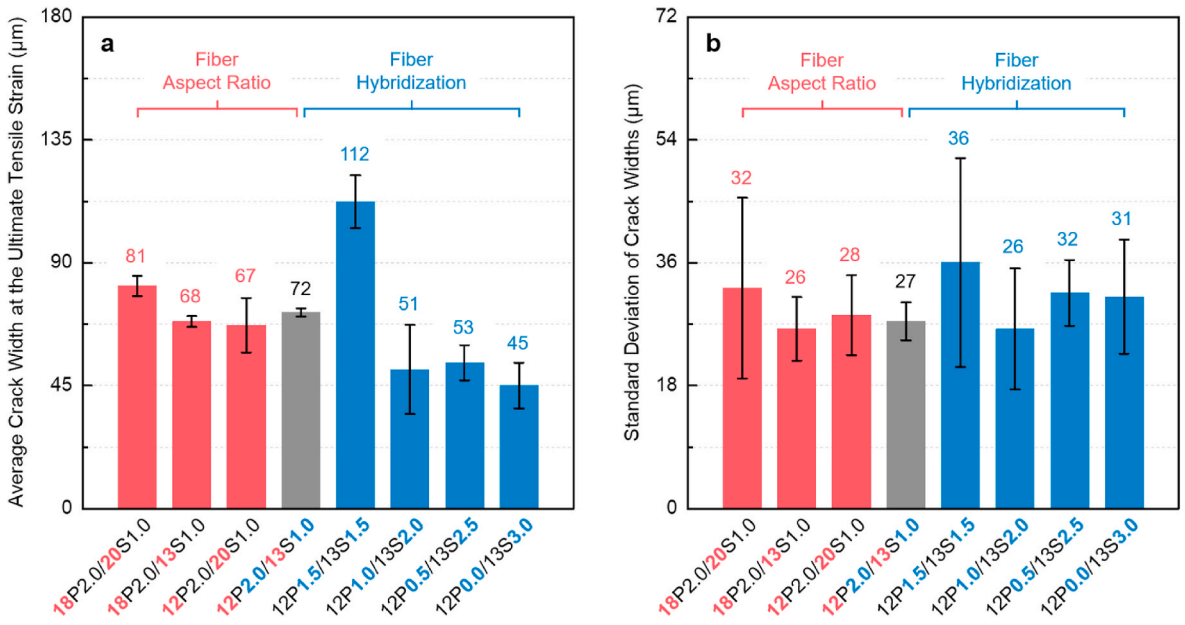

Fig. 10. Cracking behavior of UHS-ECC: (a) Average crack width at the ultimate tensile strain, and (b) standard deviation of crack widths. The mixes with steel fiber content ≥2% showed smaller crack widths. The fiber aspect ratio and hybridization had marginal effect on the standard deviation of crack widths.

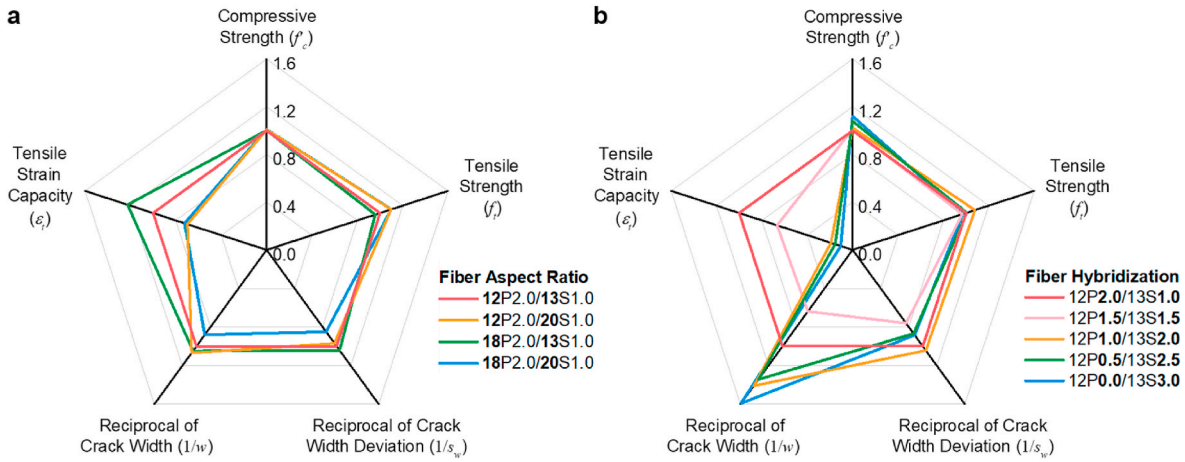

Fig. 11. Five-dimensional representation of mechanical and cracking performance of UHS-ECC: (a) Aspect-ratio series and (b) fiber-hybridization series. **18**P2.0/**13**S1.0 showed superior overall performance among all the developed UHS-ECC.

value obtained from **12P2.0/13S1.0** (i.e., the common mix for both series) for easy comparison. For the aspect-ratio series in Fig. 11a, the values of f'_c, f_t, $1/w$, and $1/s_w$ were close, and **18**P2.0/**13**S1.0 showed the highest tensile ductility and the best overall performance. For the fiber-hybridization series in Fig. 11b, the mixes with a steel fiber content ≥2% showed lower tensile ductility but higher crack resistance, and **12**P2.0/**13**S1.0 showed superior overall performance. In conclusion, the combined use of 2% PE fiber and 1% steel fiber was the best solution, and at such fiber volume ratios, the hybridization of 18-mm PE fiber and 13-mm steel fiber (i.e., **18**P2.0/**13**S1.0) showed the best overall performance of UHS-ECC among all the mixes.

5. Comparison between UHS-ECC, existing high-strength ECC, and UHPC

Table 5 summarizes the mechanical properties of high-strength ECC in existing literature, including the compressive strength f'_c, tensile strain capacity ε_t, tensile strength f_t, and average crack width w at the ultimate tensile strain. Fig. 12 shows the compressive strength *vs.* tensile strain capacity relations of the developed UHS-ECC (Table 4) and other existing ECC (Table 5). It can be found that the UHS-ECC in this research showed higher compressive strength (i.e., 211–236 MPa) than the existing ECC materials in literature. In addition, UHS-ECC showed a similar tensile ductility (3.4–6.3%) when the PE fiber content was 1.5% and above, while a significantly lower tensile ductility (i.e., 0.5–1.0%) when the PE fiber content was 1.0% or lower. In Fig. 12, ECC materials are classified as normal-strength ECC (NS-ECC, < 80 MPa in compression), high-strength ECC (HS-ECC, 80–150 MPa in compression), and ultra-high-strength ECC (UHS-ECC, ≥150 MPa in compression). Compared with existing NS- and HS-ECC, the tensile strain capacity of UHS-ECC is relatively lower (no more than 7%). In following studies, efforts can be made to further improve the tensile ductility of UHS-ECC.

The crack width deviation (i.e., s_w in Fig. 11) is not listed in Table 5 for the existing high-strength ECC, as it was not reported in most of the literature. Thus, only four dimensions [f'_c (MPa); f_t (MPa); ε_t; w (μm)] are used here to form the $f'_c f_t \varepsilon_t / w$ index (unit: MPa^2/μm) [53] to compare the overall performance (without s_w) of the present UHS-ECC and the existing high-strength ECC. The values of $f'_c f_t \varepsilon_t / w$ index of

Table 5
Mechanical properties of high-strength ECC and strain-hardening UHPC in literature.

Material	Material ID	Compressive Strength, f'_c (MPa)	Tensile Strain Capacity, ε_t (%)	Tensile Strength, f_t (MPa)	Average Crack Width, w (μm)	$f'_c f_t \varepsilon_t / w$ Index (MPa^2/μm)
High-Strength ECC in Literature	**A** (Kamal et al., 2008) [36]	96	2.8	10.0	61[a]	0.44
	B (Ranade et al., 2013) [37]	166	3.4	14.5	180	0.45
	C (Ranade 2014) [38]	205	4.6	16.1	135	1.12
	D (Curosu et al., 2017) [39]	134	3.9	7.6	68[a]	0.58
	E (He et al., 2017) [40]	153	2.3	15.0	71	0.74
	F (Chen et al., 2018) [41]	150	2.4	10.8	48[a]	0.81
	G (Yu et al., 2018) [42]	122	8.2	17.4	160[a]	1.08
	H (Lei et al., 2019) [43]	163	6.5	7.0	85	0.88
	I (Lu et al., 2019) [44]	132	6.4	10.4	58	1.52
	J (Zhang et al., 2019) [45]	87	7.0	10.9	69	0.95
	K (Li et al., 2020) [46]	131	11.0	12.1	138	1.26
	L (Nguyễn et al., 2020) [47]	104	5.3	8.0	83	0.53
	M (Zhang et al., 2020) [48]	109	3.8	13.0	78	0.70
	N (Huang et al., 2021) [4]	134	7.0	7.1	86	0.77
	O (Liu et al., 2021) [49]	130	9.7	13.5	288[a]	0.59
Strain-Hardening UHPC in Literature	**P** (Wille et al., 2014) [27]	250	0.41	19.6	12[a]	1.67
	Q (Oh et al., 2021) [29]	207	0.99	20.3	24[a]	1.73
	R (Kim et al., 2019) [30]	205	0.41	13.1	9[a]	1.22
	S (Shen et al., 2020) [31]	185	0.24	12.9	13	0.44

[a] This crack width was estimated based on the data in the corresponding reference.

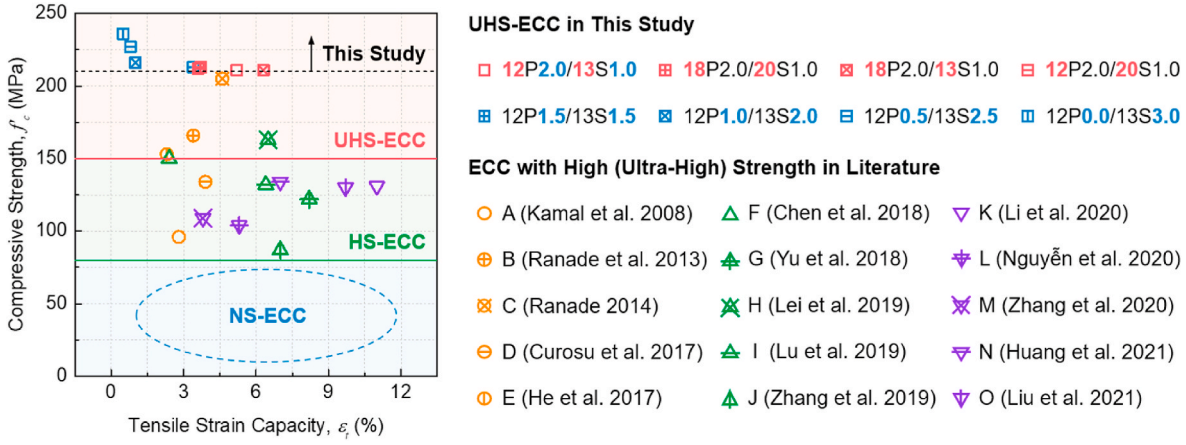

Fig. 12. Compressive strength *vs.* tensile strain capacity relations of the developed UHS-ECC and existing ECC. The developed UHS-ECC showed higher compressive strength than other existing ECC materials.

UHS-ECC and high-strength ECC are listed in Tables 4 and 5, respectively. The mechanical properties and $f'_c f_t \varepsilon_t / w$ indices of four mixes of strain-hardening UHPC in literature are also presented in Table 5 for comparison.

Fig. 13 illustrates the $f'_c f_t \varepsilon_t / w$ indices of all UHS-ECC, high-strength ECC, and strain-hardening UHPC in Tables 4 and 5. It can be found that the index values of the UHS-ECC with 2% PE fibers and 1% steel fibers (1.73–3.02 MPa^2/μm) are significantly higher than those of the other UHS-ECC mixes (0.44–1.02 MPa^2/μm). In the aspect-ratio series, the mixes with 13-mm steel fibers showed a higher index value than those with 20-mm steel fibers. Compared with existing high-strength ECC and strain-hardening UHPC, the UHS-ECC in the aspect-ratio series showed superior overall performance (with an index value $\geq$ 1.73 MPa^2/μm). In addition, among all the mixes in Figs. 13, **18**P2·0/**13**S1.0 with an index value of 3.02 MPa^2/μm recorded the best overall performance.

6. Modeling of crack width evolution of UHS-ECC

6.1. Crack width distributions at different deformation levels

In the durability design of concrete structures, the maximum crack width of the concrete cover is a critical parameter. For example, according to Chinese Standard GB/T 50,476–2019 [71], the maximum allowable crack width of concrete members in severe environment should be smaller than 0.2 mm. In addition, a crack width below 0.1 mm is preferred for the self-healing of ECC materials [11,12]. However, for cement-based composites with multiple-cracking behavior, the crack widths have considerable scatter [4,34]. Thus, it is desirable to analyze the cracking behavior of UHS-ECC based on a probabilistic-based approach. In the following, the evolution of the crack width distributions of the UHS-ECC at different deformation levels will be modeled and analyzed using the method introduced by Huang et al. [4].

For all the crack patterns shown in Fig. 9, the width of each crack was obtained by counting the pixels of the high-resolution digital images (approximately 15 μm per pixel). Then, the obtained crack widths at different deformation levels were fitted by the Weibull distributions [i.e., $F(w) = 1–\exp(–(w/\lambda)^k)$] and the fitting results are summarized in Table 6. Here, λ and k are the Weibull scale and shape parameters, respectively, w is the crack width, and r_{Fit} in Table 6 is the correlation coefficient of the Weibull best-fit result. In Table 6, it can be found that the values of r_{Fit} are close to 1, indicating that the suitability of Weibull distribution for modeling the crack width distributions of hybrid-fiber-reinforced UHS-ECC at different deformation levels.

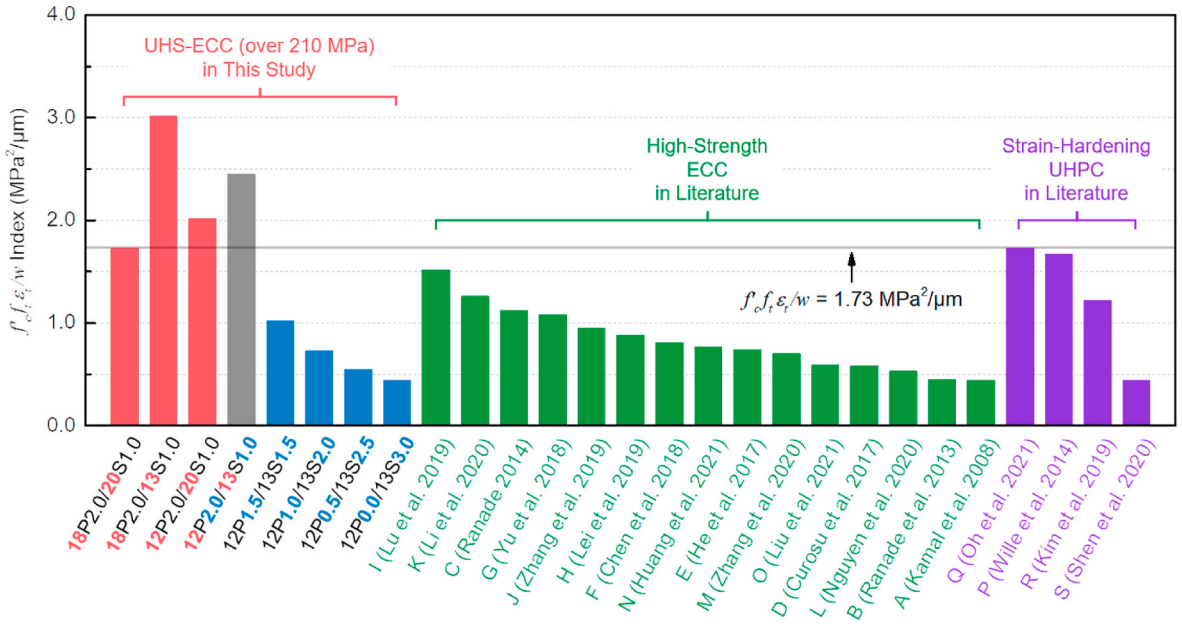

Fig. 13. Comparison of $f'_c f_t \varepsilon_t / w$ indices of UHS-ECC, high-strength ECC, and UHPC. The developed UHS-ECC with 2.0% PE fiber and 1.0% steel fiber (i.e., **18**P2.0/**20**S1.0, **18**P2.0/**13**S1.0, **12**P2.0/**20**S1.0, and **12P2.0/13S1.0**) showed higher $f'_c f_t \varepsilon_t / w$ index values than existing high-strength ECC in literature.

Table 6
Best-Fit and model results of crack width distributions at different deformation levels.

Specimen	Strain ε (%)	Best-Fit Results			Model Results			
		λ (μm)	k	r_{Fit}	λ-ε relation	λ (μm)	k	r_{Model}
18P2.0/**20**S1.0	0.20	45.3	3.03	0.866	$\lambda = 14.1\varepsilon + 42.0$ ($r = 0.98$)	44.8	$k = k_{avg}$	0.866
	1.30	57.1	2.54	0.968		60.3	$= 3.06$	0.959
	2.40	80.9	3.24	0.974		75.9		0.949
	3.50	89.1	3.44	0.981		91.4		0.979
18P2.0/**13**S1.0	0.20	43.8	3.03	0.866	$\lambda = 4.7\varepsilon + 46.7$ ($r = 0.92$)	47.7	$k = k_{avg}$	0.859
	2.27	65.0	2.02	0.980		57.3	$= 2.56$	0.968
	4.33	63.3	2.35	0.983		66.9		0.982
	6.40	76.4	2.85	0.984		76.5		0.981
12P2.0/**20**S1.0	0.20	38.4	1.69	0.940	$\lambda = 11.9\varepsilon + 46.3$ ($r = 0.83$)	48.7	$k = k_{avg}$	0.899
	1.27	74.6	2.95	0.979		61.3	$= 2.57$	0.976
	2.33	78.2	2.96	0.982		73.9		0.978
	3.40	79.3	2.69	0.986		86.6		0.985
12P2.0/13S1.0	0.20	46.7	1.56	0.866	$\lambda = 7.2\varepsilon + 46.3$ ($r = 0.99$)	47.7	$k = k_{avg}$	0.668
	1.73	60.2	3.08	0.966		58.7	$= 2.78$	0.964
	3.27	69.6	3.67	0.967		69.7		0.955
	4.80	80.2	2.81	0.984		80.7		0.984
12P**1.5**/13S**1.5**	0.20	50.2	2.29	0.999	$\lambda = 14.8\varepsilon + 59.9$ ($r = 0.88$)	62.8	$k = k_{avg}$	0.871
	1.50	98.3	3.58	0.983		82.0	$= 3.71$	0.983
	2.80	106.8	4.39	0.982		101.2		0.975
	4.10	111.3	4.60	0.977		120.4		0.970
12P**1.0**/13S**2.0**	0.20	45.3	3.03	0.866	$\lambda = 27.4\varepsilon + 37.9$ ($r = 0.98$)	43.4	$k = k_{avg}$	0.844
	0.52	50.4	1.97	0.974		52.1	$= 2.24$	0.970
	0.84	58.4	1.93	0.975		60.9		0.971
	1.16	71.8	2.05	0.984		69.6		0.981
12P**0.5**/13S**2.5**	0.20	32.5	1.46	0.996	$\lambda = 24.7\varepsilon + 31.4$ ($r = 0.85$)	36.3	$k = k_{avg}$	0.943
	0.43	48.6	1.48	0.961		42.0	$= 1.67$	0.956
	0.67	45.9	2.10	0.954		47.9		0.944
	0.90	52.7	1.65	0.987		53.6		0.987
12P**0.0**/13S**3.0**	0.20	33.4	1.86	0.946	$\lambda = 20.5\varepsilon + 29.8$ ($r = 0.85$)	33.9	$k = k_{avg}$	0.937
	0.33	35.9	1.53	0.940		36.6	$= 1.54$	0.939
	0.47	42.6	1.27	0.971		39.5		0.960
	0.60	40.2	1.49	0.959		42.1		0.959

6.2. Probabilistic modeling of crack width evolution

For the specimens in Table 6, the best-fit Weibull scale parameter λ increases as the tensile strain ε of UHS-ECC increases. In Table 6, the linear fit (i.e., $\lambda = A\varepsilon + B$) is used to describe these λ–ε relations. Here, A and B are the coefficients from the linear fitting. Fig. 14 plots the λ–ε relations of all the mixes in Table 6, and it can be seen that the linear fitting results showed good agreement with the plotted λ–ε relations. Thus, the relation $\lambda = A\varepsilon + B$ can be used in the probabilistic modeling. According to the suggestion in Ref. [4], for simplicity, the Weibull shape parameter k in the probabilistic modeling can be assumed to as a constant for each group (i.e., the average value k_{avg}).

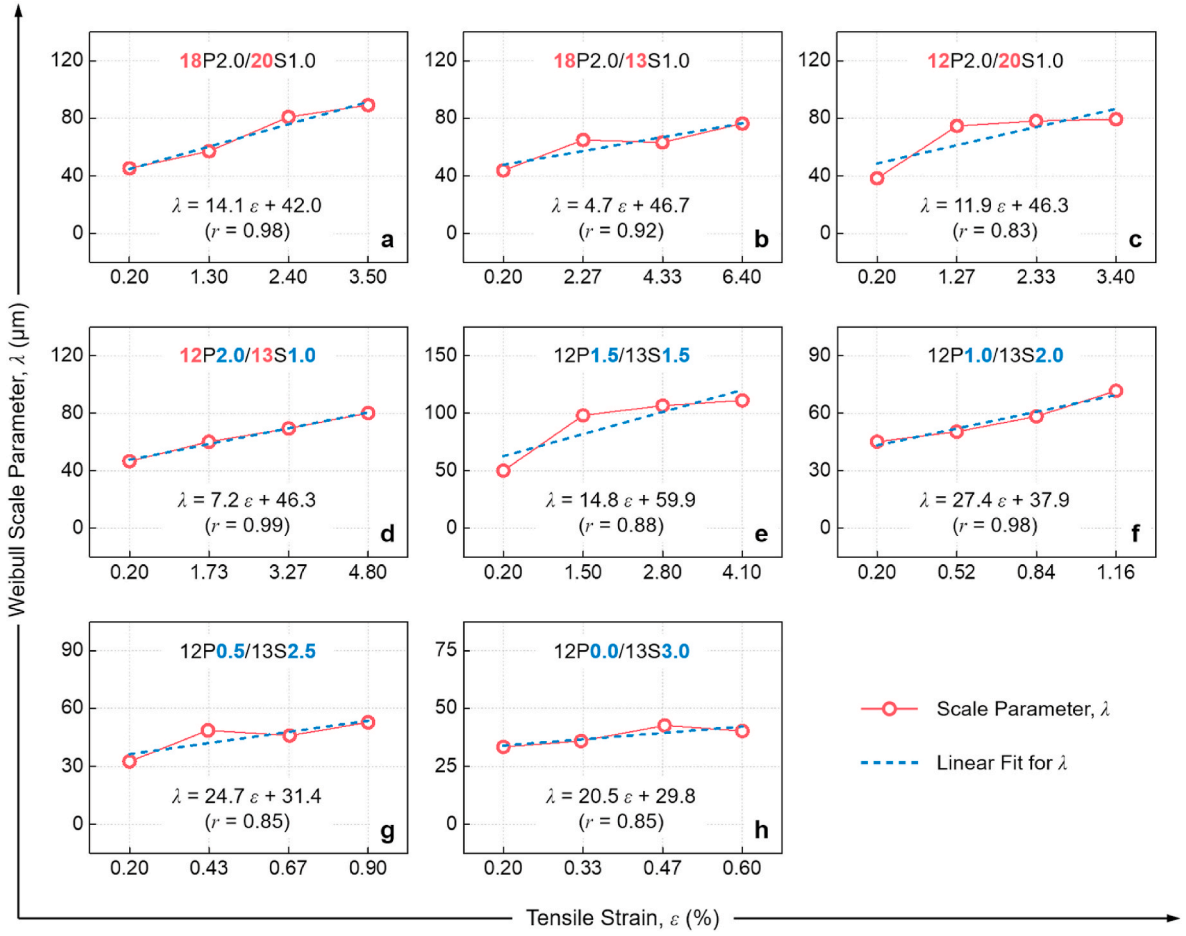

Fig. 14. The Weibull scale parameters of crack width distributions at different deformation levels. The results of linear fit showed good agreement with the measured λ–ε relation.

By introducing the equations $\lambda = A\varepsilon + B$ and $k = k_{avg}$ into the Weibull distribution of crack width [i.e., $F(w) = 1\text{–}\exp(\text{–}(w/\lambda)^k)$], the cumulative distribution of crack width w at a given tensile strain ε can be expressed as:

$$F(w) = 1 - \exp\left(- \left(\frac{w}{A\varepsilon + B}\right)^{k_{avg}}\right) \tag{2}$$

In addition, the probability density of crack width w at a given tensile strain ε can be expressed as:

$$f(w) = \left(\frac{k_{avg}}{A\varepsilon + B}\right)\left(\frac{w}{A\varepsilon + B}\right)^{k_{avg}-1} \exp\left(- \left(\frac{w}{A\varepsilon + B}\right)^{k_{avg}}\right) \tag{3}$$

It is noted that Eq. (2) and Eq. (3) can also be regarded as the cumulative distribution function and probability density function of a Weibull distribution whose scale parameter is $A\varepsilon + B$ and shape parameter is k_{avg}. Thus, based on Eq. (2) and Eq. (3), the Weibull scale and shape parameters of the crack widths distribution of UHS-ECC at different deformation levels can be obtained, and the results are also listed in Table 6 (see "Model Results") together with the correlation coefficients r_{Model}. For most cases in Table 6, the values of r_{Fit} and r_{Model} are very close, indicating that the model results showed good agreement with the best-fit results in general. Fig. 15 shows the test and model [form Eq. (3)] results of the probability density of crack width at different deformation levels. It can be found that with increasing tensile deformation levels, the average crack width increased and the variation of the crack widths became larger. In general, the model results coincided with the test results well, indicating that Eq. (3) can be applied to describe the evolution of crack width distributions of the designed UHS-ECC.

Based on Eq. (2), the tensile strain ε for a given crack width limit w and cumulative probability $F(w)$ can be calculated as follows.

$$\varepsilon = \frac{w/A}{(-\ln(1 - F(w)))^{1/k_{avg}}} - \frac{B}{A} \tag{4}$$

For comparison, the results of Eq. (4) with the cumulative probabilities of 1%, 50%, and 99% (i.e., $w_{1\%}$, $w_{50\%}$, and $w_{99\%}$) are also plotted in Fig. 15. It can be seen that most of the crack widths locate between the lines of $w_{1\%}$ and $w_{99\%}$, indicating the effectiveness of the model.

As mentioned in the beginning of this section, the maximum crack width is a critical parameter for both the durability design of concrete structures and the self-healing of ECC materials. In Fig. 15, $w_{99\%}$ could be regarded as the model results of the maximum crack widths at different deformation levels, as the cumulative probability of 99% is already a very high value. Thus, based on the result of $w_{99\%}$, the critical tensile strain of the UHS-ECC with the maximum crack width ≤100 μm (the crack width limit for excellent self-healing of ECC [11]) can be calculated (see $\varepsilon_{100\mu m}$ in Fig. 15). It can be found that the UHS-ECC with 2% PE fibers and 1% steel fibers showed higher critical tensile strain ($\varepsilon_{100\mu m}$ = 0.76–1.81%) than the other UHS-ECC mixes ($\varepsilon_{100\mu m}$ = 0.35–0.46%). In addition, for this crack width limit (100 μm), the critical tensile strain of **18**P2.0/**13**S1.0 was the highest ($\varepsilon_{100\mu m}$ = 1.81%). This finding is consistent with the results in Figs. 11 and 13 that **18**P2.0/**13**S1.0 recorded the best overall performance among the developed UHS-ECC. According to Chinese Standard GB/T 50,476–2019 [71], the maximum allowable crack width of concrete members in severe environment is 0.2 mm. For the UHS-ECC in Fig. 15, all the mixes

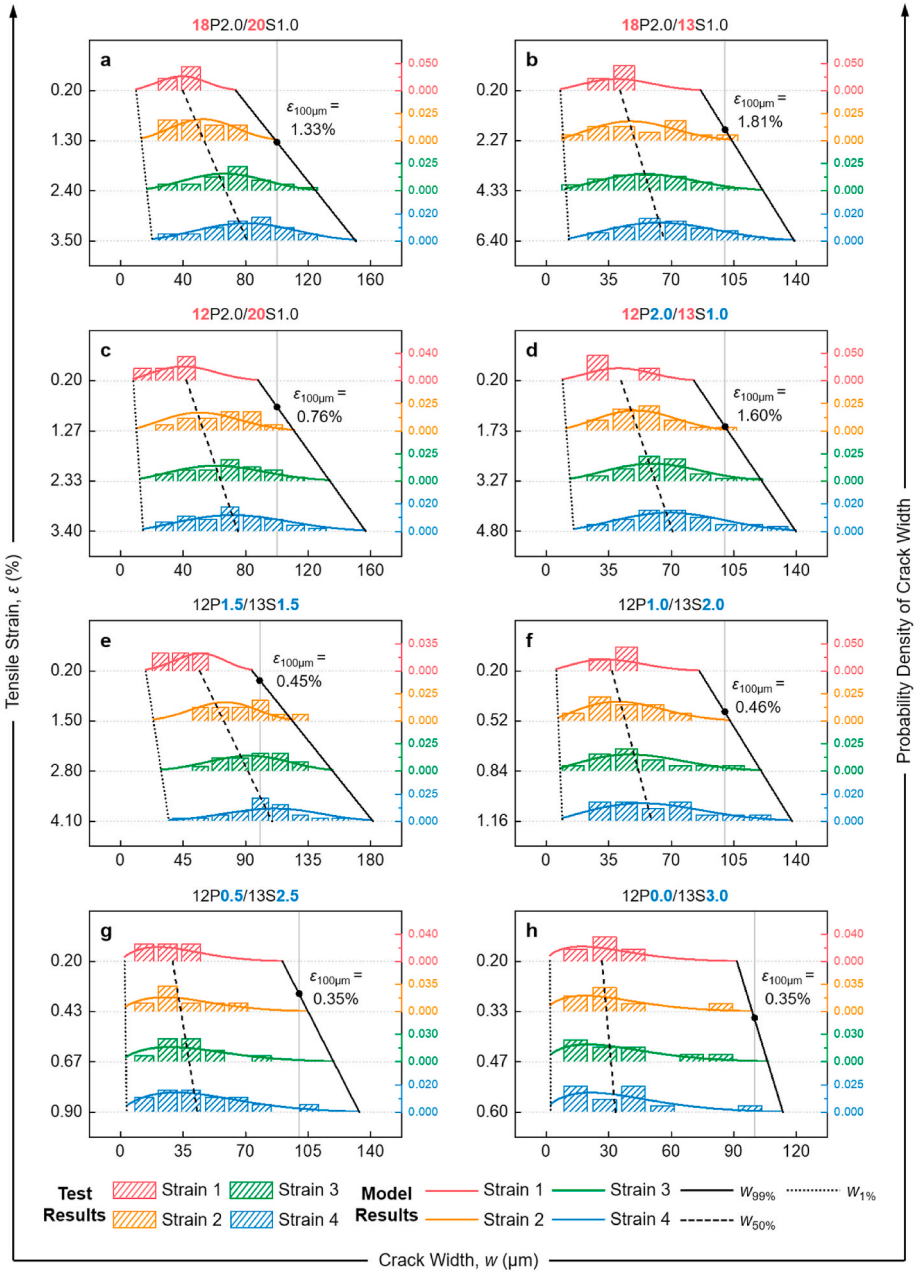

Fig. 15. The model results of the crack width distributions of UHS-ECC at different deformation levels showed good agreement with test results. For the crack width limit of 100 μm with a cumulative probability of 99% (i.e., $w_{99\%} = 100$ μm), **18**P2.0/**13**S1.0 showed the highest critical tensile strains ($\varepsilon_{100\mu m} = 1.81\%$).

had the maximum crack width well below 200 μm even at the ultimate tensile strain, indicating that the developed UHS-ECC can be applied in the concrete structures for improved durability and resilience.

7. Conclusions

In this study, a series of ultra-high-strength Engineered Cementitious Composites (UHS-ECC) with a compressive strength over 210 MPa have been developed based on the hybrid design of fiber reinforcement and matrix. The effects of fiber hybridization and aspect ratio on the mechanical properties and cracking behavior of UHS-ECC have been comprehensively investigated and analyzed. Based on the results of this study, the following conclusions can be drawn.

- A hybrid design concept has been proposed for UHS-ECC based on the combination of the packing theory of UHPC and the micromechanical principle of ECC, by which UHS-ECC with a compressive strength over 210 MPa, a tensile ductility of 3–6%, and a crack width of 67–81 μm (at the ultimate tensile strain) were achieved by the combined use of 2% polyethylene (PE) fibers and 1% steel fibers.
- For the designed UHS-ECC, the compressive strength increased with increasing the steel fiber content while the aspect ratios of PE and steel fibers had almost no effect on the compressive strength. The tensile strain capacity of UHS-ECC decreased with increasing the steel fiber content and decreasing PE fiber content given the same total fiber volumetric ratio. The crack width of the mixes with steel fiber content ≥2% showed smaller crack widths (45–53 μm at the ultimate tensile strain).
- The developed UHS-ECC showed the highest compressive strength among the existing ECC materials. Considering the mechanical properties and cracking behavior together, the combined use of 18-

mm PE fiber (2%) and 13-mm steel fiber (1%) led to the best overall performance of UHS-ECC, which exhibited higher $f'_c f_t \varepsilon_t / w$ index values (1.73–3.02 $MPa^2/\mu m$) than both high-strength ECC and strain-hardening UHPC.

- According to the probabilistic modeling, the critical tensile strain (defined as the maximum tensile deformation level with the maximum crack width $\leq$100 μm) of the UHS-ECC (with 2% PE fibers and 1% steel fibers) for the given crack width limit of 100 μm and the cumulative probability of 99% varied between 0.76% and 1.81%, which is significantly larger than the value of the other mixes (i.e, 0.35–0.46%). In addition, all the mixes showed the maximum crack width below 200 μm at the ultimate tensile strain.

CRediT author statement

BT Huang: Conceptualization, Methodology, Investigation, Visualization, Writing - Original Draft. JX Zhu: Investigation, Data Curation. KF Weng: Investigation, Validation. VC Li: Supervision, Writing - Review & Editing. JG Dai: Conceptualization, Funding Acquisition, Supervision, Writing - Review & Editing.

Declaration of competing interest

The authors declare that they have no known competing financial interests or personal relationships that could have appeared to influence the work reported in this paper.

Acknowledgments

This study was supported by financial support received from Chinese Guangdong Province R&D Plan for Key Areas (No. 2019B111107002), Hong Kong General Research Fund (RGC) (No. 15214517) and the Hong Kong Innovation and Technology Fund (No. ITS/077/18FX). Bo-Tao Huang acknowledges the support by the Hong Kong Innovation and Technology Fund through the Research Talent Hub and the support by The Hong Kong Polytechnic University through the Research Institute for Sustainable Urban Development (No.1-BBWE). The authors would also express the appreciation to Dr. Yu Xiang for helpful discussion.

References

[1] V.C. Li, Engineered Cementitious Composites (ECC) - Bendable Concrete for Sustainable and Resilient Infrastructure, Verlag GmbH Germany, Springer, Berlin, Heidelberg, 2019.
[2] V.C. Li, On engineered cementitious composites (ECC) a review of the material and its applications, J. Adv. Concr. Technol. 1 (3) (2003) 215–230.
[3] L.Y. Xu, B.T. Huang, V.C. Li, J.G. Dai, High-strength high-ductility Engineered/Strain-Hardening Cementitious Composites (ECC/SHCC) incorporating geopolymer fine aggregates, Cement Concr. Compos. 125 (2022) 104296.
[4] B.T. Huang, J.Q. Wu, J. Yu, J.G. Dai, C.K. Leung, V.C. Li, Seawater sea-sand engineered/strain-hardening cementitious composites (ECC/SHCC): assessment and modeling of crack characteristics, Cement Concr. Res. 140 (2021) 106292.
[5] L. Wang, N.U. Rehman, I. Curosu, Z. Zhu, M.A.B. Beigh, M. Liebscher, V. Mechtcherine, On the use of limestone calcined clay cement (LC3) in high-strength strain-hardening cement-based composites (HS-SHCC), Cement Concr. Res. 144 (2021) 106421.
[6] V.C. Li, C.K.Y. Leung, Steady-state and multiple cracking of short random fiber composites, J. Eng. Mech. 118 (11) (1992) 2246–2264.
[7] C.K.Y. Leung, Design criteria for pseudoductile fiber-reinforced composites, J. Eng. Mech. 122 (1) (1996) 10–18.
[8] E.H. Yang, S. Wang, Y. Yang, V.C. Li, Fiber-bridging constitutive law of engineered cementitious composites, J. Adv. Concr. Technol. 6 (1) (2008) 181–193.
[9] V.C. Li, S. Wang, C. Wu, Tensile strain-hardening behavior of polyvinyl alcohol engineered cementitious composite (PVA-ECC), ACI Mater. J. 98 (6) (2001) 483–492.
[10] J. Zhou, J. Pan, C.K. Leung, Mechanical behavior of fiber-reinforced engineered cementitious composites in uniaxial compression, J. Mater. Civ. Eng. 27 (1) (2015), 04014111.
[11] Y. Yang, M.D. Lepech, E.H. Yang, V.C. Li, Autogenous healing of engineered cementitious composites under wet–dry cycles, Cement Concr. Res. 39 (5) (2009) 382–390.
[12] S. Qian, J. Zhou, M.R. De Rooij, E. Schlangen, G. Ye, K. Van Breugel, Self-healing behavior of strain hardening cementitious composites incorporating local waste materials, Cement Concr. Compos. 31 (9) (2009) 613–621.
[13] E.N. Herbert, V.C. Li, Self-healing of microcracks in engineered cementitious composites (ECC) under a natural environment, Materials 6 (7) (2013) 2831–2845.
[14] Z. Zhang, Q. Zhang, Self-healing ability of engineered cementitious composites (ECC) under different exposure environments, *Construct. Build. Mater.* 156 (2017) 142–151.
[15] H.L. Wu, Y.J. Du, J. Yu, Y.L. Yang, V.C. Li, Hydraulic conductivity and self-healing performance of engineered cementitious composites exposed to acid mine drainage, Sci. Total Environ. 716 (2020) 137095.
[16] P. Jun, V. Mechtcherine, Behaviour of strain-hardening cement-based composites (SHCC) under monotonic and cyclic tensile loading: part 1–experimental investigations, Cement Concr. Compos. 32 (10) (2010) 801–809.
[17] B.T. Huang, Q.H. Li, S.L. Xu, W. Liu, H.T. Wang, Fatigue deformation behavior and fiber failure mechanism of ultra-high toughness cementitious composites in compression, Mater. Des. 157 (2018) 457–468.
[18] B.T. Huang, Q.H. Li, S.L. Xu, Fatigue deformation model of plain and fiber-reinforced concrete based on Weibull function, J. Struct. Eng. 145 (1) (2019), 04018234.
[19] M. Şahmaran, V.C. Li, Durability of mechanically loaded engineered cementitious composites under highly alkaline environments, Cement Concr. Compos. 30 (2) (2008) 72–81.
[20] M. Şahmaran, V.C. Li, Durability properties of micro-cracked ECC containing high volumes fly ash, Cement Concr. Res. 39 (11) (2009) 1033–1043.
[21] H. Liu, Q. Zhang, V. Li, H. Su, C. Gu, Durability study on engineered cementitious composites (ECC) under sulfate and chloride environment, Construct. Build. Mater. 133 (2017) 171–181.
[22] K. Rokugo, T. Kanda, H. Yokota, N. Sakata, Applications and recommendations of high performance fiber reinforced cement composites with multiple fine cracking (HPFRCC) in Japan, Mater. Struct. 42 (9) (2009) 1197.
[23] B.T. Huang, Q.H. Li, S.L. Xu, C.F. Li, Development of reinforced ultra-high toughness cementitious composite permanent formwork: experimental study and digital image correlation analysis, Compos. Struct. 180 (2017) 892–903.
[24] B.T. Huang, J.G. Dai, K.F. Weng, J.X. Zhu, S.P. Shah, Flexural performance of UHPC-Concrete-ECC composite member reinforced by perforated steel plate, J. Struct. Eng. 147 (6) (2020), 04021065.
[25] B.T. Huang, Q.H. Li, S.L. Xu, B. Zhou, Strengthening of reinforced concrete structure using sprayable fiber-reinforced cementitious composites with high ductility, Compos. Struct. 220 (2019) 940–952.
[26] P. Richard, M. Cheyrezy, Composition of reactive powder concretes, Cement Concr. Res. 25 (7) (1995) 1501–1511.
[27] K. Wille, S. El-Tawil, A.E. Naaman, Properties of strain hardening ultra high performance fiber reinforced concrete (UHP-FRC) under direct tensile loading, Cement Concr. Compos. 48 (2014) 53–66.
[28] B.T. Huang, J.X. Zhu, K.F. Weng, J.Q. Huang, J.G. Dai, Prefabricated UHPC-Concrete-ECC underground utility tunnel reinforced by perforated steel plate: experimental and numerical investigations, Case Studies in Construction Materials (2021), e00856.
[29] T. Oh, I. You, N. Banthia, D.Y. Yoo, Deposition of nanosilica particles on fiber surface for improving interfacial bond and tensile performances of ultra-high-performance fiber-reinforced concrete, Compos. B Eng. (2021) 109030.
[30] M.J. Kim, D.Y. Yoo, Y.S. Yoon, Effects of geometry and hybrid ratio of steel and polyethylene fibers on the mechanical performance of ultra-high-performance fiber-reinforced cementitious composites, J. Mater. Res. Technol. 8 (2) (2019) 1835–1848.
[31] X. Shen, E. Brühwiler, Influence of local fiber distribution on tensile behavior of strain hardening UHPFRC using NDT and DIC, Cement Concr. Res. 132 (2020) 106042.
[32] J.G. Dai, B.T. Huang, S.P. Shah, Recent advances in strain-hardening UHPC with synthetic fibers, Journal of Composites Science 5 (10) (2021) 283.
[33] J. Li, Z. Wu, C. Shi, Q. Yuan, Z. Zhang, Durability of ultra-high performance concrete–A review, Construct. Build. Mater. 255 (2020) 119296.
[34] B.T. Huang, Y.T. Wang, J.Q. Wu, J. Yu, J.G. Dai, C.K. Leung, Effect of fiber content on mechanical performance and cracking characteristics of ultra-high-performance seawater sea-sand concrete, Adv. Struct. Eng. 24 (6) (2020) 1182–1195.
[35] H. Huang, X. Gao, L. Teng, Fiber alignment and its effect on mechanical properties of UHPC: an overview, Construct. Build. Mater. 296 (2021) 123741.
[36] A. Kamal, M. Kunieda, N. Ueda, H. Nakamura, Evaluation of crack opening performance of a repair material with strain hardening behavior, Cement Concr. Compos. 30 (10) (2008) 863–871.
[37] R. Ranade, V.C. Li, M.D. Stults, W.F. Heard, T.S. Rushing, Composite properties of high-strength, high-ductility concrete, ACI Mater. J. 110 (4) (2013) 413–422.
[38] R. Ranade, Advanced Cementitious Composite Development for Resilient and Sustainable Infrastructure, Ph.D. Thesis, University of Michigan, 2014.
[39] I. Curosu, M. Liebscher, V. Mechtcherine, C. Bellmann, S. Michel, Tensile behavior of high-strength strain-hardening cement-based composites (HS-SHCC) made with high-performance polyethylene, aramid and PBO fibers, Cement Concr. Res. 98 (2017) 71–81.
[40] S. He, J. Qiu, J. Li, E.H. Yang, Strain hardening ultra-high performance concrete (SHUHPC) incorporating CNF-coated polyethylene fibers, Cement Concr. Res. 98 (2017) 50–60.
[41] Y. Chen, J. Yu, C.K. Leung, Use of high strength strain-hardening cementitious composites for flexural repair of concrete structures with significant steel corrosion, Construct. Build. Mater. 167 (2018) 325–337.

[42] K.Q. Yu, J.T. Yu, J.G. Dai, Z.D. Lu, S.P. Shah, Development of ultra-high performance engineered cementitious composites using polyethylene (PE) fibers, Construct. Build. Mater. 158 (2018) 217–227.
[43] D.Y. Lei, L.P. Guo, B. Chen, I. Curosu, V. Mechtcherine, The connection between microscopic and macroscopic properties of ultra-high strength and ultra-high ductility cementitious composites (UHS-UHDCC), Compos. B Eng. 164 (2019) 144–157.
[44] Z. Lu, J. Yao, C.K. Leung, Using graphene oxide to strengthen the bond between PE fiber and matrix to improve the strain hardening behavior of SHCC, Cement Concr. Res. 126 (2019) 105899.
[45] Z. Zhang, A. Yuvaraj, J. Di, S. Qian, Matrix design of light weight, high strength, high ductility ECC, Construct. Build. Mater. 210 (2019) 188–197.
[46] Y. Li, X. Guan, C. Zhang, T. Liu, Development of high-strength and high-ductility ECC with saturated multiple cracking based on the flaw effect of coarse river sand, J. Mater. Civ. Eng. 32 (11) (2020), 04020317.
[47] H.H. Nguyễn, J.I. Choi, S.E. Park, S.L. Cha, J. Huh, B.Y. Lee, Autogenous healing of high strength engineered cementitious composites (ECC) using calcium-containing binders, Construct. Build. Mater. 265 (2020) 120857.
[48] Z. Zhang, F. Yang, J.C. Liu, S. Wang, Eco-friendly high strength, high ductility engineered cementitious composites (ECC) with substitution of fly ash by rice husk ash, Cement Concr. Res. 137 (2020) 106200.
[49] T. Liu, R. Bai, Z. Chen, Y. Li, Y. Yang, Tailoring of polyethylene fiber surface by coating silane coupling agent for strain hardening cementitious composite, Construct. Build. Mater. 278 (2021) 122263.
[50] B.T. Huang, J. Yu, J.Q. Wu, J.G. Dai, C.K. Leung, Seawater sea-sand Engineered Cementitious Composites (SS-ECC) for marine and coastal applications, Composites Communications 20 (2020) 100353.
[51] B.T. Huang, J.Q. Wu, J. Yu, J.G. Dai, C.K. Leung, High-strength seawater sea-sand Engineered Cementitious Composites (SS-ECC): mechanical performance and probabilistic modeling, Cement Concr. Compos. 114 (2020) 103740.
[52] Y. Zhou, B. Xi, K. Yu, L. Sui, F. Xing, Mechanical properties of hybrid ultra-high performance engineered cementitious composites incorporating steel and polyethylene fibers, Materials 11 (8) (2018) 1448.
[53] B.T. Huang, K.F. Weng, J.X. Zhu, Y. Xiang, J.G. Dai, V.C. Li, Engineered/strain-hardening cementitious composites (ECC/SHCC) with an ultra-high compressive strength over 210 MPa, Composites Communications 26 (2021) 100775.
[54] M. Khan, M. Cao, M. Ali, Effect of basalt fibers on mechanical properties of calcium carbonate whisker-steel fiber reinforced concrete, Construct. Build. Mater. 192 (2018) 742–753.
[55] M. Khan, M. Cao, M. Ali, Cracking behaviour and constitutive modelling of hybrid fibre reinforced concrete, J. Build. Eng. 30 (2020) 101272.
[56] M. Maalej, S.T. Quek, S.F.U. Ahmed, J. Zhang, V.W.J. Lin, K.S. Leong, Review of potential structural applications of hybrid fiber Engineered Cementitious Composites, Construct. Build. Mater. 36 (2012) 216–227.
[57] M.J. Kim, D.Y. Yoo, Y.S. Yoon, Effects of geometry and hybrid ratio of steel and polyethylene fibers on the mechanical performance of ultra-high-performance fiber-reinforced cementitious composites, J. Mater. Res. Technol. 8 (2) (2019) 1835–1848.
[58] J. Yu, Y. Chen, C.K. Leung, Mechanical performance of Strain-Hardening Cementitious Composites (SHCC) with hybrid polyvinyl alcohol and steel fibers, Compos. Struct. 226 (2019) 111198.
[59] R. Yu, P. Spiesz, H.J.H. Brouwers, Mix design and properties assessment of ultra-high performance fibre reinforced concrete (UHPFRC), Cement Concr. Res. 56 (2014) 29–39.
[60] Z. Wu, C. Shi, K.H. Khayat, Influence of silica fume content on microstructure development and bond to steel fiber in ultra-high strength cement-based materials (UHSC), Cement Concr. Compos. 71 (2016) 97–109.
[61] J.E. Funk, D.R. Dinger, Predictive Process Control of Crowded Particulate Suspensions: Applied to Ceramic Manufacturing, Kluwer Academic Publishers, Boston, United States, 2013.
[62] ASTM C1437, Standard Test Method for Flow of Hydraulic Cement Mortar, ASTM International, West Conshohocken, PA, 2020.
[63] M. Li, V.C. Li, Rheology, fiber dispersion, and robust properties of engineered cementitious composites, Mater. Struct. 46 (3) (2013) 405–420.
[64] C. Shi, D. Wang, L. Wu, Z. Wu, The hydration and microstructure of ultra high-strength concrete with cement–silica fume–slag binder, Cement Concr. Compos. 61 (2015) 44–52.
[65] ASTM C109/C109M, Standard Test Method for Compressive Strength of Hydraulic Cement Mortars, ASTM International, West Conshohocken, PA, 2013.
[66] Japan Society of Civil Engineers, Recommendations for Design and Construction of High Performance Fiber Reinforced Cement Composites with Multiple Fine Cracks (HPFRCC), Concrete Engineering Series No, 2008, p. 82.
[67] L.Y. Xu, B.T. Huang, J.G. Dai, Development of engineered cementitious composites (ECC) using artificial fine aggregates, Construct. Build. Mater. 305 (2021) 124742.
[68] Q.H. Li, X. Yin, B.T. Huang, A.M. Luo, Y. Lyu, C.J. Sun, S.L. Xu, Shear interfacial fracture of strain-hardening fiber-reinforced cementitious composites and concrete: a novel approach, Eng. Fract. Mech. 253 (2021) 107849.
[69] T.F. Yuan, J.Y. Lee, Y.S. Yoon, Enhancing the tensile capacity of no-slump high-strength high-ductility concrete, Cement Concr. Compos. 106 (2020) 103458.
[70] K. Yu, Y. Ding, Y.X. Zhang, Size effects on tensile properties and compressive strength of engineered cementitious composites, Cement Concr. Compos. 113 (2020) 103691.
[71] Chinese Standard GB/T 50476-2019, Standard for Design of Concrete Structure Durability, Ministry of Housing and Urban-Rural Development of the People's Republic of China, Beijing, China, 2019 (In Chinese).